

pubs.acs.org/JACS Article

Turning 2D MOFs into Mixed Ionic-Electronic Conductors via Side Chain Engineering

Heejung Roh, Alice Y. Su, Changhwan Oh, Julius J. Oppenheim, Heather J. Kulik, Aristide Gumyusenge,* and Mircea Dincă*



Cite This: J. Am. Chem. Soc. 2025, 147, 38419–38427



ACCESS

III Metrics & More

Article Recommendations

Supporting Information

ABSTRACT: Despite the wide-ranging use of metal—organic frameworks (MOFs) as either electronic or ionic conductors, mixed electron—ion conductivity in MOFs remains largely unexplored. Here, we report a new methodology for designing new mixed ionic electronic conductors (MIECs) by tethering ionophilic ethylene glycol (EG) functional groups onto an electrically conductive MOF (cMOF), yielding $M_3(HIR_3\text{-TAT})_2$ (M = Ni, Cu; TAT = triazatruxene; R = nBu, 1EG, 2EG; referred to as M-R). Leveraging systematic physicochemical variability in the pore microenvironment while preserving in-plane conjugation of the functionalizable TAT core, we orthogonally tune and enhance electronic conjugation through the crystalline framework (in-plane and out-of-plane) and ionic transport through defined abundant pore



channels. Upon LiTFSI incorporation, Ni-1EG exhibits the highest room-temperature ionic conductivity $(1.1 \times 10^{-4} \text{ S/cm})$ in the series—nearly an order of magnitude higher than Ni-nBu $(4.18 \times 10^{-5} \text{ S/cm})$, which features a hydrophobic side chain of the same length—while preserving the electronic conductivity $(\sim 5 \times 10^{-4} \text{ S/cm})$. Consistent with previous reports, the added steric bulk in Ni-2EG reduces electronic conductivity to $2.7 \times 10^{-4} \text{ S/cm}$, though the drop is minimal compared to aliphatic side chains of similar length. Counterintuitively, despite improved polarity, ionic conductivity significantly decreases in Ni-2EG, to $2.58 \times 10^{-6} \text{ S/cm}$, likely due to pore blockage, with electronic conductivity largely remaining unchanged at $2.7 \times 10^{-6} \text{ S/cm}$. This study unlocks the potential of cMOFs as tunable platforms for the decoupled control of ionic and electronic transport via side chain engineering. It opens doors to the unexplored design space of single-phase porous crystalline MIECs with orthogonal integration of functionalities tailored for emerging applications in chemistry, physics, and materials science.

■ INTRODUCTION

Mixed ionic-electronic conductive materials (MIECs) are of interest for a variety of applications across energy storage, electrocatalysis, memristors, chemiresistors, and bioelectronics. 1-7 In all of these applications, the general working mechanism requires conductive materials that respond electronically to ionic fluxes or vice versa. A major research challenge remains around achieving balanced ionic and electronic conduction within a single material, thereby eliminating the need for additives and composites. Conductive metal-organic frameworks (cMOFs), composed of π -conjugated ligands and metal ions forming van der Waals-stacked two-dimensional (2D) layers, have recently emerged as promising MIECs. Their long-range order enables high electronic conductivity via in-plane π -conjugation and out-ofplane orbital overlap along the framework (i.e., through-bond and through-space, respectively), while their abundant yet defined pore channels support efficient ionic transport.^{8–13}

Unlike conventional semicrystalline or amorphous organic MIECs, where ionic conductivity is enhanced through bulk

swelling, often disrupting the crystalline domains that underpin electronic conjugation, MOFs hold potential for intrinsic orthogonality of transport pathways. 10,11,14 That is, by leveraging ionic transport via side chain-modulated pore environment (*e.g.*, polarity, pore size) and electronic transport through the framework (*i.e.*, in-plane π -d conjugation and out-of-plane π - π stacking), the electronic conjugation can be largely preserved even upon tethering ionophilic side chains onto otherwise hydrophobic frameworks. With this property, cMOFs are promising in terms of overcoming the trade-off between the two modes of transport as well as their simultaneous optimization in a single material.

Received: July 10, 2025 Revised: September 10, 2025

Accepted: September 14, 2025 Published: September 22, 2025





Despite their conceptual promise and wide-ranging use as either electronic or ionic conductors, mixed ionic-electronic conduction in MOFs has remained largely unexplored. Notably, a recent work has shown dual proton-electron conduction in single-phase three-dimensional (3D) MOFs via uncoordinated hydroquinone, highlighting the potential of functional group design for dual transport.¹⁵ Furthermore, recent studies on triazatruxene (TAT)-based 2D cMOFs have shown that side chain functionalization with aliphatic groups of varying lengths can tune interlayer spacing by introducing steric hindrance while preserving in-plane conjugation. ¹⁶ In TAT MOFs, specific surface area and pore preoccupancy characterizations revealed that the side chains reside mainly within the pores. Notably, tuning of the interlayer spacing can be executed orthogonally to in-plane electronic conjugation. This strategy has been leveraged to precisely modulate spin concentration, Seebeck coefficients in thermoelectrics, and faradaic contributions in pseudocapacitors. $^{16-18}$

These early successes encouraged us to explore synthetic approaches that allow installation of side chains, giving systematic insight into decoupling electronic and ionic conduction. Here, we present a molecular design strategy to enhance mixed conduction in cMOFs through side chain engineering, leveraging orthogonal control over ionic and electronic transport within an electrically conjugated, crystalline porous framework. Specifically, we employ ethylene glycol (EG) side chains, commonly used in physical mixtures with electrodes to enhance ion solvation and mobility while also mitigating interfacial incompatibility that hinders charge transfer at the electrolyte-electrode interface in solid-state electrochemical systems. 19 To our knowledge, this represents the first crystalline, side chain-functionalized cMOF deliberately designed as a mixed ionic-electronic conductor, in contrast to prior systems studied primarily as either ionic, electronic, or more recently protonic dual conductors.

■ RESULTS AND DISCUSSION

Scheme 1 shows the MOF structures investigated in this study. Truxene, a heptacyclic polyarene with C_{3h} symmetry, is selected as the ligand due to its versatility as a building block for assembling MOFs with functionalizability at three nitrogen sites, offering rare opportunities for targeted side chain incorporation in cMOFs. Starting from the reported hydrophobic *n*-butyl (*n*Bu) side chain, ¹⁶ we synthesized counterparts with polar side chains with comparable and increased length. Ethylene glycol (EG) is chosen for its polarity and conformational flexibility, which promote dynamic reorientation and facilitate ion transport. 20-23 Commonly used for enhancing ion solvation and reducing interfacial resistance in solid-state systems, EG also improves compatibility by mitigating charge transfer resistance at the electrode–electrolyte interface. ^{12,23,24} We hypothesize that introducing a two-carbon spacer between the framework and the first ether oxygen electronically decouples the side chain from the conjugated backbone, minimizing possible disruption to the framework's electronic conjugation. Additionally, as reported in other systems, electrostatic interactions between EG side chains may help preserve framework integrity by offsetting the steric bulk of longer side chains.²⁵

Prior reports suggesting that increasing side chain length can cause interlayer expansion, disrupt π - π stacking, reduce conductivity, and even hinder MOF formation prompted the initial conduct of *in silico* geometry optimizations. We thus

Scheme 1. Structures Targeted for Studying the Impact of Side Chain Engineering on Ionic and Electronic Conduction in cMOFs

used the Forcite module in Materials Studio 2020^{26} with the universal force field (UFF), where the geometry was optimized to the minimum energy configuration to determine the upper limit of side chain length that could reasonably fit into an assembled framework (Figures 1 and S1–S3). We found that side chains extending beyond two EG units would lead to significant interlayer expansion. Modeling a single EG side chain resulted in a slightly reduced interlayer distance (4.166 Å) compared to the aliphatic butyl counterpart (4.183 Å), suggesting that incorporation of a single ether oxygen should introduce significant polarity without disrupting interlayer $\pi-\pi$ interactions.

Doubling the aliphatic chain length from butyl to octyl was predicted to lead to a substantial increase in interlayer distance to 4.406 Å (a 0.223 Å jump), whereas extending the chain from 1EG to 2EG caused only a marginal change, promising minimal disruption to framework packing (Figures S3 and S4). Notably, extension to 3EG groups resulted in a pronounced increase in the simulated stacking distance to 4.289 Å. Corresponding $2 \times 2 \times 1$ supercells illustrate the extent of pore occupancy by varied side chains (Figure S5). With these predictions in hand, we focused our study on Ni- and Cu-based materials functionalized with nBu, 1EG, and 2EG side chains. Nickel and copper were chosen, given the extensive literature covering the superior electrical properties of cMOFs made with these metal ions. 27

Solvothermal reaction between metal precursors (nickel acetate, copper sulfate) and a series of functionalized hexaaminotriazatruxene (HATAT) ligands in water/N,N-dimethylformamide/N,N-dimethylacetamide with a sodium acetate modulator yields a series of six HATAT-based hexagonal 2D layered cMOFs with the general formula $M_3(HIR_3-TAT)_2$ (M=Ni, Cu; R=-nBu, -1EG, -2EG; herein abbreviated as M-R) (Scheme 1). Details on synthetic aspects, including elemental analysis, NMR, and other physicochemical characterization, are provided in the Supporting Information (Figures S1 and S6–S8). Fourier-transform infrared (FTIR) spectroscopy of all six materials shows the disappearance of the N-H stretching band observed in the

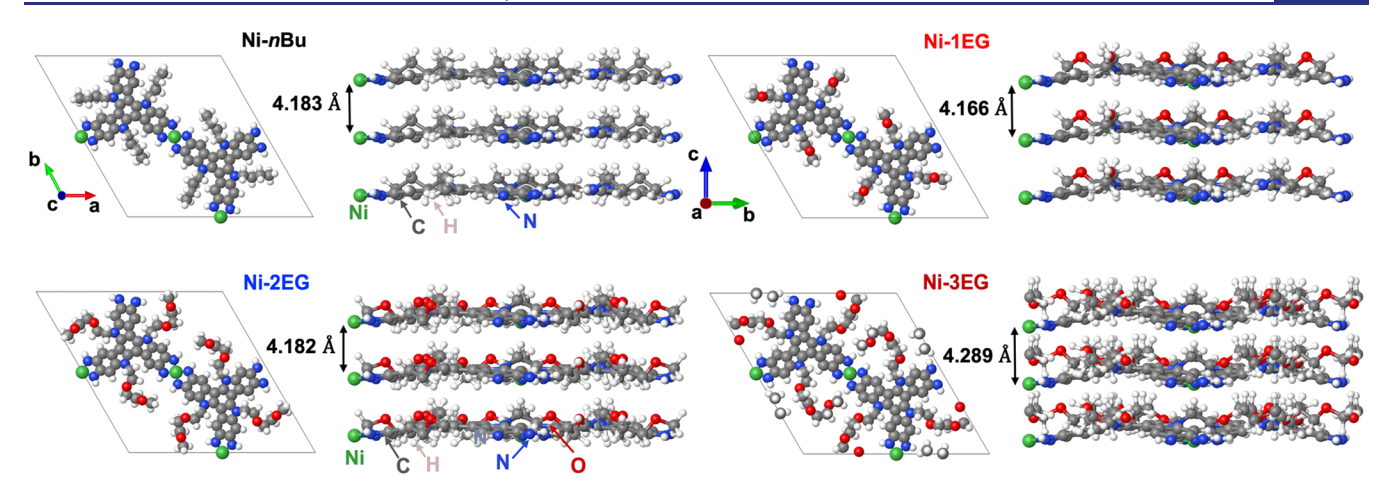


Figure 1. Illustration of Ni-MOFs showing the evolution of simulated interlayer spacing as a function of side chains. Geometry was optimized using a Forcite module (universal force field) in Materials Studio. The modeled crystal structure is shown along the *c* direction and parallel to the *ab* plane. Gray, red, blue, and green spheres represent C, O, N, and Ni atoms, respectively.

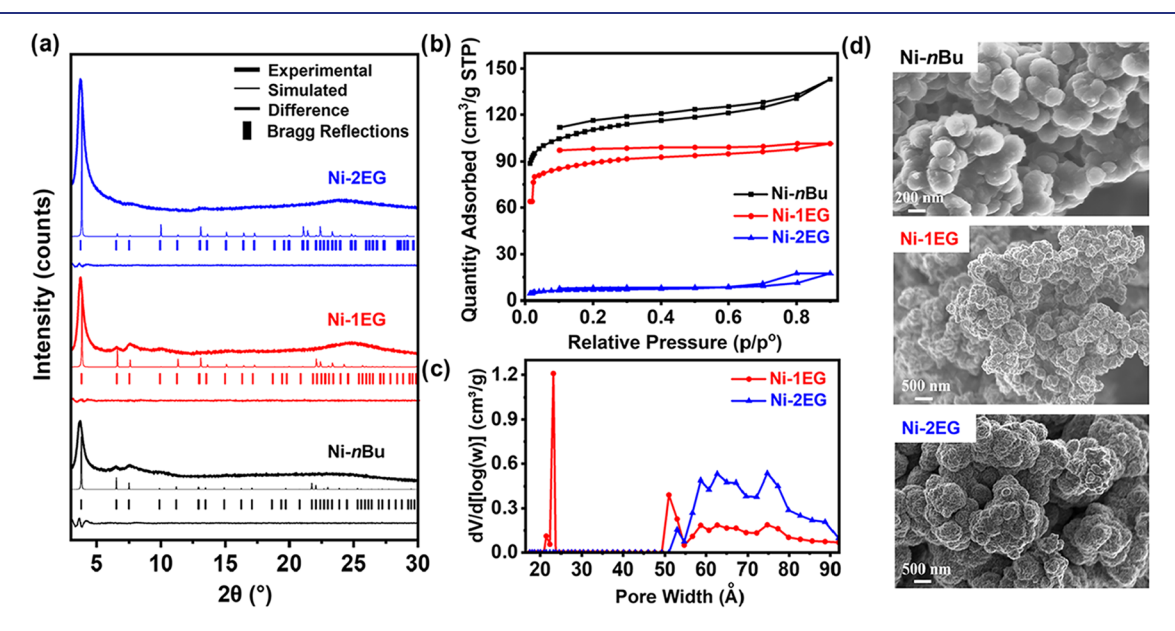


Figure 2. (a) Experimental and simulated PXRD patterns for Ni-MOFs with varying side chains. (Details on Pawley refinement and difference curves can be found in Figure S13.) (b) N₂ sorption isotherms of the Ni-MOFs with varying side chains. (c) Barrett–Joyner–Halenda (BJH) model fitted incremental pore size exhibiting pore size distributions. (d) SEM images of Ni-MOFs with varied side chains.

free ligands (Figure S7), confirming successful coordination polymerization, consistent with previous reports on 2D TAT-based cMOFs. ¹⁷ C–H stretching bands from the side chains (2800–3000 cm⁻¹) are observed in all MOFs, confirming side chain incorporation (Figure S8). The spectrum of the only previously reported material, Ni-nBu, matches well with literature data. ^{16,17} MOFs with EG side chains (Ni/Cu-1EG and Ni/Cu-2EG) exhibit slightly different peak-splitting profiles, likely due to electron-withdrawing effects from ether oxygen atoms. Additionally, the higher relative intensities of C–H stretching modes in 2EG-tethered MOFs compared to 1EG are consistent with the greater number of carbon atoms in the longer side chain.

The structures of the newly synthesized MOFs were first validated, and the conditions were optimized (Figures S9 and S10) by powder X-ray diffraction (PXRD), which revealed characteristic 2θ reflections at ~ 3.7 , ~ 6.5 , $\sim 7.5^{\circ}$, and a broader peak between ~ 23 and 27° for both Ni- (Figure 2a) and Cubased MOFs (Figure S11). These values are consistent with

those previously reported for the aliphatic MOF families and match simulated patterns (Figure S12).¹⁶ Pawley refinement of the experimental PXRD patterns (see difference patterns in Figures 2a and S13) confirmed strong agreement between the simulated and experimental structures, with extracted values of $R_{\rm wp}$ = 2.18% and $R_{\rm p}$ = 1.70% for Ni-1EG, $R_{\rm wp}$ = 2.63% and $R_{\rm p}$ = 2.08% for Ni-2EG, and R_{wp} = 3.07% and R_p = 2.45% for Ni*n*Bu. Refined data and values (R_{wp}, R_p) for Cu-MOFs are given in Figure S13. As side chains become longer and bulkier, overcrowding leads to pore saturation and compromised framework integrity, ultimately hindering MOF formation. Indeed, all attempts to obtain Ni-3EG yielded essentially amorphous powders (Figure S14), evidenced by the decay of the [100] reflection at $2\theta = \sim 3.7^{\circ}$ and the broadening and shift of the out-of-plane [001] reflection at $2\theta = \sim 25^{\circ}$, indicating disrupted interlayer stacking and reduced in-plane order. This steric limitation appears more pronounced in the Cu analogue, as evidenced by the faster degradation of the in-plane peak at $\sim 3.7^{\circ}$ in Cu-2EG. Similarly, the out-of-plane peak becomes

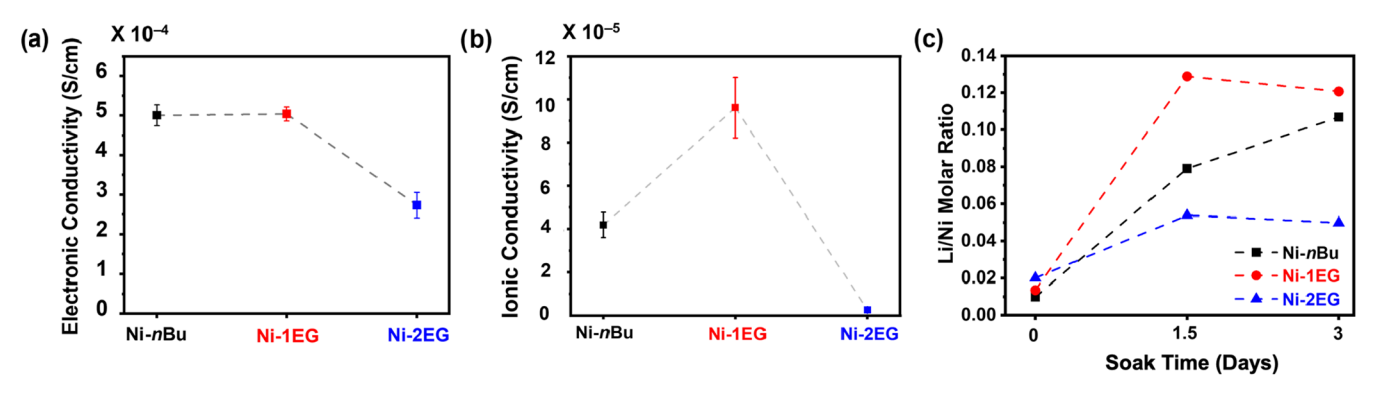


Figure 3. (a) Measured electrical conductivity of Ni-MOFs with varied side chains. (b) Measured ionic conductivity of Ni-MOFs with varied side chains after equilibrium. For the measurement, samples were presoaked in 1 M LiTFSI in propylene carbonate (PC) electrolyte for 3 days. (c) Saturated molar ratio collected from ICP-MS after soaking Ni-MOFs in 1 M LiTFSI in PC electrolyte. Note: The *x*-axis starts at day 0, which denotes the baseline background in ICP-MS measurements.

significantly broadened and shifted, indicating increased structural disorder (Figure S14). This underscores the metal-dependent side chain effect and intricate interplay between metal and ligand for the resulting conjugation. Despite a less pronounced compromise in integrity than that of completely amorphous Ni-3EG, Cu-2EG was excluded from further characterization to avoid confusion.

Interlayer stacking distances along the c direction were determined experimentally from the [001] reflections in the 2θ = $23-28^{\circ}$ range (Figure 2a). When nBu is replaced with 1EG and 2EG side chains, the interlayer distances remain nearly constant in Ni-MOFs, measured as 3.7, 3.5, and 3.7 Å for NinBu, Ni-1EG, and Ni-2EG, respectively, consistent with simulation trends (Figure S15 and Table S1). Cu-MOFs showed a similar trend, with interlayer distances of 3.8, 3.6, and 4.0 Å for Cu-nBu, Cu-1EG, and Cu-2EG, respectively (Figure S16 and Table S2). Notably, in both cases, the equivalent length of the ionophilic side chain (Ni-1EG and Cu-1EG) compared to their aliphatic counterpart (Ni-nBu and Cu-nBu) maintained interlayer packing. Ni-MOFs also show comparable in-plane ordering, with the full-width at half-maximum (FWHM) of the [100] reflection at $2\theta = 3.76^{\circ}$ measured to be ~0.49-0.50° (Figure S17 and Table S3). Similarly, Cu analogues show comparable FWHM values of ~0.50-0.51° (Figure S18 and Table S4). These results indicate that crystallinity is preserved with polar EG side chains, though the effect diminishes with increasing chain length. The enhanced crystallinity likely arises from electrostatic interactions between EG moieties and their ability to bend, reducing steric interference and promoting closer interlayer spacing, in accordance with previous reports on 2D MOFs, ^{28,29} as well as polymeric MIECs, ^{23,30,31} upon systematic optimization of length and placement. For instance, glycolated polymers exhibit distinctive side chain interdigitation and packing conformations not seen in alkylated analogues.²³ However, it is worth noting that in polymer MIECs, long and floppy side chains often disrupt $\pi - \pi$ stacking and increase amorphousness, which can facilitate ion insertion but compromise electronic transport, ^{23,32–34} highlighting the inherent trade-offs between side chain selection and ionic-electronic conduction.

 N_2 sorption isotherms at 77 K measured on activated cMOFs (Figure 2b,c) revealed decreasing porosity with increasing side chain length. In contrast, porosity seems unaffected by the polarity of the side chain. Thus, Brunauer–Emmett–Teller (BET) surface areas were calculated as 377 \pm

 $9 \text{ m}^2/\text{g}$ for Ni-nBu, $269 \pm 5 \text{ m}^2/\text{g}$ for Ni-1EG, and $21 \pm$ $0.6 \,\mathrm{m}^2/\mathrm{g}$ for Ni-2EG (Figure 2b). Pore size distributions obtained from fitting the N2 isotherms to the Barrett-Joyner-Halenda (BJH) model (Figure 2b,c) revealed that substituting the hydrophobic butyl group with polar EG side chains preserved pore accessibility in Ni-1EG, with a pore width peaking around $\sim 20-22$ Å. However, in the case of Ni-2EG, only intergrain (meso)porosity was detected (>50-90 Å), which is also shown for Ni-1EG, further supporting the BET results indicating that longer EG side chains block the MOF's pores and render them inaccessible to neutral gaseous guests (Figure 2c). High-resolution X-ray photoelectron spectra (XPS) of the Ni(2p) region confirm the presence of Ni²⁺ in all Ni-MOFs (Ni-nBu, Ni-1EG, Ni-2EG), as indicated by the Ni 2_{p3/2} binding energy (BE) of 856 eV (Figure S19), consistent with previous reports. 15 The presence of two peaks in the Cu(2p) BEs region corresponding to 2p_{3/2} at 934.10 eV and $2p_{1/2}$ at 953.97 eV ($\Delta SO \approx 19.87$ eV) for $Cu^{\scriptscriptstyle +}$ and $2p_{3/2}$ at 936.33 eV and $2p_{1/2}$ at 956.24 eV ($\Delta SO \approx 19.91 \text{ eV}$) for Cu^{2+} , indicate Cu²⁺/Cu⁺ mixed valency in the Cu-MOFs (Figure S20). Scanning electron microscopy (SEM) revealed cauliflower-like morphologies (Figure 2c), consistent with previously reported structures of analogous cMOFs. 16

Thermogravimetric analysis (TGA) revealed that both Ni-1EG and Ni-2EG begin to lose significant mass above 200 °C (Figure S21). Ni-1EG decomposes more gradually and retains a higher residual mass, indicating greater thermal resistance, compared to Ni-2EG, which exhibits sharp and pronounced weight loss. This difference can be attributed to the increased degrees of freedom from the longer, more flexible side chains, consistent with previous reports linking greater molecular flexibility to lower decomposition temperatures due to enhanced segmental motion and entropy-driven destabilization.³⁵ Variable-temperature PXRD (VT-PXRD) was employed to further evaluate the thermal stability of Ni-1EG. The material retained its characteristic diffraction peaks up to 250 °C under ambient air, beyond which complete decay was observed (Figure S22). While heat resistance is desirable for solid-state electrochemical applications such as solid-state batteries (SSBs), ^{36,37} it remains rare for cMOFs to be stable under both heat and ambient conditions.33

Experimentally measured two-probe electronic conductivities averaged over four measurements are the following (in 10^{-4} S/cm): 5.001 \pm 0.026, 5.033 \pm 0.0058, and 2.733 \pm 0.032 for Ni-nBu, Ni-1EG, and Ni-2EG, respectively (Figure

3a). Compared to nBu, conductivity remained unchanged with 1EG and decreased by less than half with 2EG, despite the incorporation of 6 7-atom-long side chains per pore. This is notable given that a similar length of aliphatic chains often disrupts MOF formation (Figures S4 and S14). The result aligns with prior reports of EG chains promoting electrostatic stacking, 28,29 likely acting as interlayer anchors that mitigate steric repulsion and help preserve electronic conductivity. Cubased MOFs showed approximately 3 orders of magnitude lower electrical conductivity than those of Ni-based counterparts: 1.62×10^{-6} S/cm, 4.83×10^{-7} S/cm, and 8.65×10^{-8} S/cm for Cu-nBu, Cu-1EG, and Cu-2EG, respectively (Figure S23). This large conductivity gap of several orders of magnitude is consistent with previous findings in aminobridged and diamine-linked frameworks, including Ni₃(HITP)₂ and Ni₃(HITT)₂, outperforming their Cu analogues.^{9,27} This is attributed to stronger in-plane metal-ligand overlap in Ni frameworks, while Cu analogues rely more on out-of-plane π - π stacking, where interlayer disruptions more severely impact conductivity, explaining the significant drop in Cu-2EG rendered nearly insulating, also highlighting the critical interplay between side chains and metal node in electronic transport. From a coordination chemistry perspective, Ni nodes form more covalent interactions with the diaminobenzene moiety, resulting in significantly stronger in-plane π -d conjugation, more dispersive electronic bands, and a higher density of charge carriers. In contrast, Cu frameworks form more ionic bonds with weaker orbital overlaps, producing less dispersive in-plane bands and greater charge localization; as a result, in-plane conjugation contributes less to conductivity than out-of-plane stacking, making Cu systems more sensitive to disruptions in interlayer order.²⁷ Thus, it is noteworthy that the side chain trends do not necessarily transfer across different metal nodes, and intrinsic metal-ligand electronic interplay sets the baseline conductivity in 2D diamine-linked cMOFs.

Diffuse-reflectance ultraviolet-visible-near IR (DRUV-vis-NIR) spectroscopic characterizations of six MOFs further corroborate the discussed effect of side chain and metal node on electrical conductivity. All Ni-MOFs (Ni-nBu, Ni-1EG, Ni-2EG) exhibit significantly stronger absorption in the lowenergy (NIR) range than Cu-MOFs (Cu-nBu, Cu-1EG, Cu-2EG), suggesting that the degree of in-plane π -d electronic delocalization in Ni-MOFs is significantly higher than that in Cu-MOFs and is indicative of stronger electronic coupling between Ni²⁺ and diamine ligands regardless of side chains, aligning with superior electrical conductivity observed across Ni-MOFs. Instead, a characteristic peak at 580-600 nm observed in all Cu-MOFs (Figure S24) matches previous reports of Cu-diamine MOFs, 16 which is attributed to intervalence charge transfer (IVCT) between Cu⁺ and Cu²⁺ centers. The coexistence of both oxidation states is further confirmed by XPS (Figure S20), thus supporting the proposed mechanistic differences. This ability to tune conductivity by orders of magnitude through metal node substitution reflects the ligand's modularity for tailored electronic design and indicates that metal-ligand pairing influences side chain effects on mixed conduction.

Ionic conductivity was measured via AC methods^{38,39} after soaking the three Ni-MOFs in 1 M lithium bis-(trifluoromethylsulfonyl)imide (LiTFSI) solution in propylene carbonate (PC), followed by filter-washing and drying to generate LiTFSI-Ni-MOFs (*i.e.*, Li–Ni-nBu, Li–Ni-1EG, Li–Ni-2EG). Preloading with LiTFSI (particularly Li⁺ ions) is a

common strategy to enhance ionic conductivity in solid-state electrolytes by increasing mobile ion density. 19,40 Inductively coupled plasma mass spectrometry (ICP-MS) was employed to quantify the amount of lithium incorporated in each framework through the Li/Ni molar ratios in the LiTFSI-Ni-MOFs samples. Saturated Li/Ni molar ratios (R) after 3 days of LiTFSI soaking (Figure 3c) show a side chain-dependent trend: $R_{\rm Ni-1EG}=0.12069>R_{\rm Ni-nBu}=0.10679>R_{\rm Ni-2EG}=0.04978$. Although both Ni-1EG and Ni-nBu exhibit preserved porosity, the higher R in Ni-1EG highlights the role of side chain polarity in enhancing salt uptake. However, the more polar Ni-2EG exhibited the lowest Li⁺ uptake, approximately three times lower than that of Ni-1EG, likely due to pore blockage that restricts guest access.

FTIR spectroscopy was used to compare LiTFSI-Ni-MOFs with their pristine counterparts (Figure S25) to confirm the presence of residual ions, identify changes in bonding environments, if any, and assess how ion uptake varies with side chain chemistry, factors likely influencing ionic conductivity. The presence of Li⁺ and TFSI⁻ in Ni-MOFs was confirmed by a peak at ~750 cm⁻¹, corresponding to the CF₃ bending mode of TFSI-. This band appears only after LiTFSI soaking in Ni-1EG and Ni-nBu but is absent in the case of Ni-2EG. This suggests that ions are retained in the pores of Ni-1EG and Ni-nBu, whereas uptake is suppressed due to pore blockage in Ni-2EG, resulting in complete ion removal during washing. This is corroborated by the C-H stretching region (2800-3000 cm⁻¹) where Ni-1EG and Ni-nBu show additional shoulders after soaking, indicating conformational changes upon ion insertion which is absent in Ni-2EG, likely due to the low amount of TFSI present. Notably, only LiTFSI-Ni-1EG exhibits splitting of the CH₂ scissoring peak (~1430 cm⁻¹) into multiple peaks (1400–1500 cm⁻¹), indicating chemically distinct environments and strong, diverse Li⁺ interactions along the side chains (Figure S25). These features, less pronounced in 2EG and absent in the nBu analogue, further support Ni-1EG's superior ion uptake and its ability to form spacious, ion-accessible coordination environments. Together, the absence of TFSI- and unchanged C-H profiles in Ni-2EG support a reduction in ion uptake, while spectral changes in Ni-1EG and Ni-nBu confirm ion entrapment within the pore structure. Ionic conductivity followed the trend Ni-1EG > Ni-nBu > Ni-2EG, with measured average values of 9.61×10^{-5} S/cm (with the highest reaching $\sim 1.1 \times 10^{-5}$ 10^{-4} S/cm), 4.18×10^{-5} S/cm, and 2.58×10^{-6} S/cm, respectively (Figures 3b and S26). Once saturation was reached, extending the soaking time had a minimal effect (Figure S27). Across all side chains, Ni-MOFs exhibited consistent features in EIS: Ri scaled linearly with film thickness $(R^2 > 0.99, Figure S28)$, and spectra showed a single semicircle (bulk ionic resistance) followed by a long capacitive tail, indicative of blocked electron transfer (Figure S26). The voltage-dependent tail slope, with Ri remaining unchanged (Figure S29), further confirms that Ri reflects bulk ion transport.

To better isolate the side chain's influence on ionic conductivity, we normalized conductivity values by the respective Li/Ni molar ratios (R), thereby accounting for differences in residual Li⁺ content. Using Ni-2EG as the reference ($R_{\text{Ni-2EG}} = 0.04978$ is reset to 1 as $R_{\text{Ni-2EG}} = 1$), the remaining normalized R values (R') are $R_{\text{Ni-nBu}}' = 2.14$ and $R_{\text{Ni-1EG}}' = 2.42$, both relative to Ni-2EG. Dividing the measured ionic conductivities of 9.61×10^{-5} S/cm for Ni-

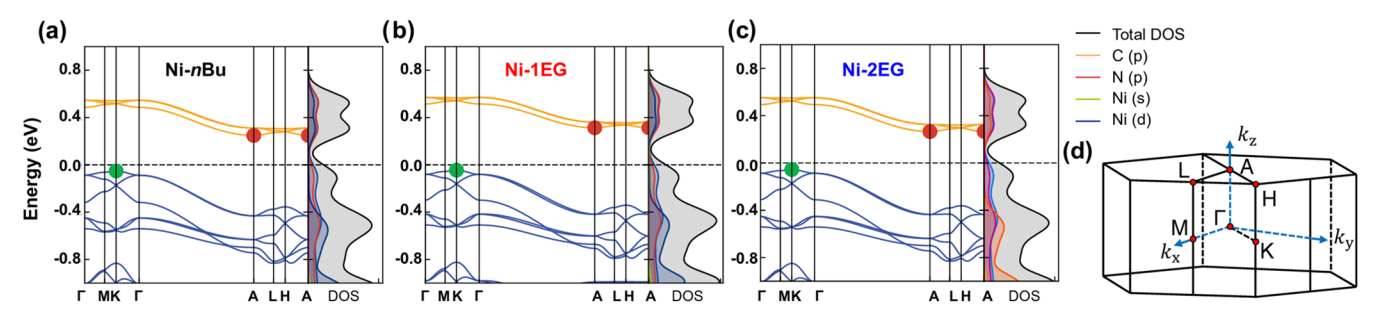


Figure 4. Effect of polar side chains on electrical conductivity in Ni-based conductive MOFs. Calculated band structure and density of states of Ni-MOFs; Ni-nBu (a), Ni-1EG (b), and Ni-2EG (c). High-symmetry points in the first Brillouin zone are sampled, including in-plane points (Γ , M, and K) and out-of-plane points (Λ , L, and H). The valence and conduction bands are depicted as blue and orange solid lines, respectively. In each plot, the valence band maximum (VBM) and conduction band minimum (CBM) are marked with green and red circles, respectively. The orange, red, light green, and dark blue denote Γ , Ni(Γ), and Ni(Γ), respectively. (d) Brillouin surface of hexagonal space group Γ 0. High-symmetry points Γ (0, 0, 0), M (1/2, 0, 0), K (1/3, 1/3, 0), L (1/2, 0, 1/2), A (0, 0, 1/2), and H (1/3, 1/3, 1/2), used in the band structure calculation, are marked with red circles. The reciprocal lattice vectors Γ 1. Γ 2 are indicated with blue arrows.

1EG, 4.18×10^{-5} S/cm for Ni-nBu, and 2.58×10^{-6} S/cm for Ni-2EG by their respective Li/Ni molar ratios (2.42, 2.14, and 1) yields normalized ionic conductivity values of 3.97×10^{-5} , 1.95×10^{-5} , and 2.58×10^{-6} S/cm, respectively. These results confirm that Ni-1EG maintains the highest intrinsic ionic conductivity, even after accounting for differences in Li⁺ uptake. The consistent trend across normalized values confirms that differences in ionic conductivity arise not merely from variations in ion loading but are fundamentally driven by structural and chemical effects of the side chains.

To further validate the intrinsic differences in transport for the series of MOFs, pristine Ni-MOFs without LiTFSI presoaking were tested using a battery-like setup, adopting a modified Hebb-Wagner polarization method with LilSSEI MIEClLi architecture where the lithium metal electrode serves as the Li⁺ source, and solid-state electrolyte (SSE) is utilized for an electron-transfer blocking layer (Figure S30). 39,41,42 The same trend is observed with ionic conductivities of 4.4 \times 10 $^{-6}$ S/cm, 1.01 \times 10 $^{-5}$ S/cm, 6.28 \times 10 $^{-6}$ S/cm for Ni-nBu, Ni-1EG, and Ni-2EG, respectively. The absolute values are approximately an order of magnitude lower compared to the values extracted from AC methods, 38,39 likely due to reduced density of mobile ions in this configuration.

The superior ionic conductivity of Ni-1EG is attributed to its ability to introduce additional ionic hopping sites and enhance ionophilicity while preserving sufficient porosity for ion uptake. In contrast, the longer 2EG side chains, despite greater polarity and flexibility, primarily block pores through steric bulk, as confirmed by BET analysis, leading to a significant difference in ionic conductivity. While other effects of excess EG-such as ion trapping through coordination, reduced segmental mobility, or local phase separation—may also play roles, steric hindrance provides the most consistent explanation for the significant decrease in ionic conductivity of Ni-2EG. Similar disproportionate effects of subtle side chain modifications (e.g., a one-carbon difference), drastically altering interlayer spacing and electrochemical response, have been reported in TAT frameworks, 16,17 which also aligns with our back-of-theenvelope calculation of geometric pore blockage. The significant drop from 1EG to 2EG in saturated Li/Ni ratio and the increased peak intensity of residual LiTFSI in ex situ FTIR further corroborate steric restriction as the evident factor limiting ion uptake (i.e., carrier density) and thus ionic conductivity.

While Ni-2EG shows only a minor decrease in the electronic conductivity, it exhibits drastically reduced ionic conductivity. Ni-1EG, by contrast, achieves an optimal balance of polarity, porosity, and interlayer spacing, reaching an ionic conductivity of 1.1×10^{-4} S/cm. Supporting this, Ni-1EG exhibits a higher specific capacity than Ni-2EG in cyclic voltammetry using a 1 M LiClO₄ aqueous electrolyte (Figures S31 and S32), measured with a scan rate of 2, 5, 10, and 20 mV/s in a voltage window of 0.6-1 V vs Ag/Ag+ using a three-electrode supercapacitor setup. The rectangular CV profiles indicate predominantly capacitive charge storage. The higher capacitance observed for Ni-1EG is attributed to its greater accessible pore volume and efficient transport compared with Ni-2EG. To evaluate side chain effects on dispersibility in polar solvents, we used acetone and water for dynamic light scattering (DLS) measurements (Figure S33). Among the Ni-MOFs, Ni-1EG exhibited the highest dispersibility, with the smallest cluster sizes (\sim 20 nm in acetone; \sim 3.5 nm and 200 nm in water), indicating enhanced compatibility with polar molecules, consistent with its highest observed ionic conductivity. Ni-2EG showed intermediate cluster sizes (~150 nm in acetone; \sim 20 and 600 nm in water), while Ni-nBu displayed the poorest dispersibility (~420 nm in acetone; ~250 nm and 1000 nm in water). Thus, the highest dispersibility observed in Ni-1EG again indicates that both ionophilicity and the preserved porosity are critical. Collectively, the comparable surface area to its hydrophobic counterpart (BET), distinctive features arising from additional chemical interaction with intercalated ions only appearing in Ni-1EG (FTIR), and the highest Li/Ni ratio in LiTFSI-Ni-1EG (ICP-MS) confirm significant Li+ incorporation in Ni-1EG, the highest among the series, attributed to its balanced pore accessibility and ion compatibility. These results demonstrate that the 1EG side chain achieves optimal ionic conduction by balancing preserved porosity and enhanced ionophilicity, providing ample hopping sites for ion transport and improved solvation for capacitive storage, outperforming the nBu analogue while avoiding the pore-blocking effects observed with 2EG.

DFT calculations using semilocal plane-wave were performed to further improve estimates of the equilibrium structure and evaluate band structures of the 2D cMOFs. All atomic positions and cell parameters were relaxed to estimate interlayer distances, which showed a slight increase, less than 0.04 Å, with a two times increase in side chain length from 1EG to 2EG. Aliphatic side chains appeared to result in even

larger interlayer spacing (4.1308 Å for Ni-nBu) than the glycol counterpart (4.0118 Å for Ni-1EG and 4.0501 Å for Ni-2EG), which is consistent with the modeled crystal structures in Figure 1, suggesting that EG chains may form tighter packing, potentially due to favorable interchain interactions or reduced steric hindrance. Further details on optimized structures are given in Table S5. Band structures computed from the optimized geometries exhibit a flat band across the Brillouin zone and a Dirac cone at the K point (Figures 4a–c and S34). The flat band structures along in-plane symmetry directions $(\Gamma - M - K - \Gamma)$ reflect degenerate and localized electronic eigenstates, which implies a high effective mass of the charge carriers within the 2D layers. Further details on band structure calculation can be found in Figures S34 and S35. Band gap energies were determined from the energy difference between the valence band maximum (VBM) and the conduction band minimum (CBM) of each structure. All 2D cMOFs revealed no band crossing the Fermi level and displayed semiconducting behavior with narrow band gaps ranging from 0.30 to 0.43 eV. The band dispersion near the Fermi level remained largely unchanged across three structures. These calculations align with experimental results, showing that interlayer spacing, conjugation, and electronic conductivity are minimally affected by substituting hydrophobic (nBu) with ionophilic (1EG) side chains and even with extended 2EG chains. Alongside sterically modulated interlayer spacing, inductive effects represent another pathway through which side chains can influence electrical conductivity. By positioning the heteroatoms (O atoms) two carbons away from the conjugated backbone (i.e., honeycomb-like skeleton), the framework's π -conjugation is preserved by minimizing electronic perturbation from the side chains.

CONCLUSIONS

While there is potential for orthogonality between ionic and electronic transport pathways in cMOFs, offering a unique opportunity to overcome conventional trade-offs, mixed ionicelectronic conductive MOFs remain largely unexplored. We leverage a porous crystalline framework and enhance mixed ionic-electronic transport by tethering ionophilic EG side chains onto TAT ligands in $M_3(HIR_3-TAT)_2$ (M = Ni, Cu; R = nBu, 1EG, 2EG) 2D cMOFs. We systematically investigate how side chain polarity and length modulate interlayer spacing, pore microenvironments, and transport properties. In Ni-based MOFs, replacing aliphatic nBu with 1EG side chains significantly enhances ionic conductivity $(1.1 \times 10^{-4} \text{ S/cm})$, nearly an order of magnitude higher than Ni-nBu (4.18×10^{-5}) S/cm), while maintaining electronic conductivity (\sim 5 × 10⁻⁴ S/cm). This enhancement arises from increased hopping site density as well as the ionophilic and electrolyte-like coatings within pores that promote solvation and Li⁺ transport without compromising crystallinity and pore accessibility.

By contrast, extending to 2EG reduces ionic conductivity $(2.58 \times 10^{-6} \text{ S/cm})$ due to pore blockage, with only a slight decline in electronic transport (2.7 \times 10⁻⁴ S/cm). Excessive side chain length imposes steric hindrance that negates polarity benefits, underscoring the need for balanced side chain design. Ni-1EG thus strikes the optimal balance of ionic accessibility/ uptake, structural order, and mobility-critical factors for solid-state ionic conduction, outperforming both hydrophobic and longer polar analogues. At the same time, Ni-1EG preserves electronic conductivity by maintaining crystallinity and in-plane/out-of-plane conjugation, evidenced by the

preserved interlayer distance. Finally, we show that the MOF's intrinsic modularity enables facile tuning of conductivity over orders of magnitude simply by switching the metal node (e.g., Ni vs Cu).

In this work, we establish a molecular design strategy for the orthogonal tuning of ionic and electronic transport in cMOFs. We show that systematic side chain engineering enables decoupled control and optimization of ionic conductivity (via pore chemistry and porosity) and electronic conjugation (through in-plane π -d decolocalization and out-of-plane π - π stacking), overcoming the trade-offs common in organic analogues. To our knowledge, this represents the first crystalline, porous, side chain-functionalized cMOF deliberately designed as an intrinsic MIEC, distinct from recent dual conductors limited to protons. This work opens a new design space for single-phase porous crystalline MIECs relevant for a variety of applications and fundamental studies.

ASSOCIATED CONTENT

Supporting Information

The Supporting Information is available free of charge at https://pubs.acs.org/doi/10.1021/jacs.5c11806.

Materials and methods; synthetic procedures; material characterization details; simulations; supporting figures and tables (PDF)

AUTHOR INFORMATION

Corresponding Authors

Aristide Gumyusenge – Department of Materials Science and Engineering, Massachusetts Institute of Technology, Cambridge, Massachusetts 02139, United States; orcid.org/0000-0003-4995-5222; Email: aristide@ mit.edu

Mircea Dinca – Department of Chemistry, Massachusetts Institute of Technology, Cambridge, Massachusetts 02139, *United States;* orcid.org/0000-0002-1262-1264; Email: mdinca@mit.edu

Authors

Heejung Roh - Department of Materials Science and Engineering, Massachusetts Institute of Technology, Cambridge, Massachusetts 02139, United States; Department of Chemistry, Massachusetts Institute of Technology, Cambridge, Massachusetts 02139, United States Alice Y. Su - Department of Chemistry, Massachusetts Institute of Technology, Cambridge, Massachusetts 02139, United States

Changhwan Oh - Department of Materials Science and Engineering, Massachusetts Institute of Technology, Cambridge, Massachusetts 02139, United States; Department of Chemical Engineering, Massachusetts Institute of Technology, Cambridge, Massachusetts 02139, United States; o orcid.org/0000-0003-2120-6676

Julius J. Oppenheim – Department of Chemistry, Massachusetts Institute of Technology, Cambridge, Massachusetts 02139, United States; oorcid.org/0000-0002-5988-0677

Heather J. Kulik - Department of Chemical Engineering and Department of Chemistry, Massachusetts Institute of Technology, Cambridge, Massachusetts 02139, United States; orcid.org/0000-0001-9342-0191

Complete contact information is available at:

https://pubs.acs.org/10.1021/jacs.5c11806

Author Contributions

The manuscript was written through the contributions of all authors. All authors have given approval to the final version of the manuscript.

Notes

The authors declare no competing financial interest.

ACKNOWLEDGMENTS

H.R. acknowledges the Surpina and Panos Eurnekian Nanotechnology Fund Fellowship from MIT. A.S. and M.D. acknowledge the Department of Energy (DE-SC0023288) for financial support. H.R., A.G., H.J.K., and C.O. acknowledge support in the form of a seed grant from the Abdul Latif Jameel Water & Food Systems (JWAFS) Lab at MIT. Part of this work made use of the Shared Experimental Facilities including the Materials Research Laboratory (MRL) and the Department of Chemistry Instrumentation Facility (DCIF) at MIT. We thank Dr. Juan Felipe Torres Gonzalez, Zhentao Yang, Dr. Jiande Wang, and Dr. Hanyu Liu for their insightful discussions.

REFERENCES

- (1) Riess, I. Mixed Ionic-Electronic Conductors—Material Properties and Applications. *Solid State Ionics* **2003**, *157* (1), 1–17.
- (2) Chen, C.-C.; Fu, L.; Maier, J. Synergistic, Ultrafast Mass Storage and Removal in Artificial Mixed Conductors. *Nature* **2016**, *536* (7615), 159–164.
- (3) Li, J.; Wang, C.; Su, J.; Liu, Z.; Fan, H.; Wang, C.; Li, Y.; He, Y.; Chen, N.; Cao, J.; Chen, X. Observing Proton—Electron Mixed Conductivity in Graphdiyne. *Adv. Mater.* **2024**, *36* (25), No. 2400950.
- (4) Sood, A.; Poletayev, A. D.; Cogswell, D. A.; Csernica, P. M.; Mefford, J. T.; Fraggedakis, D.; Toney, M. F.; Lindenberg, A. M.; Bazant, M. Z.; Chueh, W. C. Electrochemical Ion Insertion from the Atomic to the Device Scale. *Nat. Rev. Mater.* **2021**, *6* (9), 847–867.
- (5) Hatakeyama, K.; Tateishi, H.; Taniguchi, T.; Koinuma, M.; Kida, T.; Hayami, S.; Yokoi, H.; Matsumoto, Y. Tunable Graphene Oxide Proton/Electron Mixed Conductor That Functions at Room Temperature. *Chem. Mater.* **2014**, *26* (19), 5598–5604.
- (6) Tan, S. T. M.; Gumyusenge, A.; Quill, T. J.; LeCroy, G. S.; Bonacchini, G. E.; Denti, I.; Salleo, A. Mixed Ionic–Electronic Conduction, a Multifunctional Property in Organic Conductors. *Adv. Mater.* **2022**, 34 (21), No. 2110406.
- (7) Paulsen, B. D.; Tybrandt, K.; Stavrinidou, E.; Rivnay, J. Organic Mixed Ionic-Electronic Conductors. *Nat. Mater.* **2020**, *19* (1), 13–26
- (8) Liu, L.; Xu, Q.; Zhu, Q.-L. Electrically Conductive Metal—Organic Frameworks for Electrocatalytic Applications. *Adv. Energy Sustainable Res.* **2021**, 2 (11), No. 2100100.
- (9) Sun, L.; Campbell, M. G.; Dincă, M. Electrically Conductive Porous Metal—Organic Frameworks. *Angew. Chem., Int. Ed.* **2016**, *55* (11), 3566–3579.
- (10) Kharod, R. A.; Andrews, J. L.; Dincă, M. Teaching Metal-Organic Frameworks to Conduct: Ion and Electron Transport in Metal-Organic Frameworks. *Annu. Rev. Mater. Res.* **2022**, 52 (52, 2022), 103–128.
- (11) Ribeiro, C.; Tan, B.; Figueira, F.; Mendes, R. F.; Calbo, J.; Valente, G.; Escamilla, P.; Paz, F. A. A.; Rocha, J.; Dincă, M.; Souto, M. Mixed Ionic and Electronic Conductivity in a Tetrathiafulvalene-Phosphonate Metal—Organic Framework. *J. Am. Chem. Soc.* **2025**, 147 (1), 63—68.
- (12) Sadakiyo, M.; Yamada, T.; Kitagawa, H. Rational Designs for Highly Proton-Conductive Metal—Organic Frameworks. *J. Am. Chem. Soc.* **2009**, *131* (29), 9906—9907.

- (13) da Silva, R. M. L.; Albano, L. G. S.; Vello, T. P.; de Araújo, W. W. R.; de Camargo, D. H. S.; Palermo, L. D.; Corrêa, C. C.; Wöll, C.; Bufon, C. C. B. Surface-Supported Metal-Organic Framework as Low-Dielectric-Constant Thin Films for Novel Hybrid Electronics. *Adv. Electron. Mater.* **2022**, 8 (9), No. 2200175.
- (14) Jo, Y.-M.; Kim, D.-H.; Wang, J.; Oppenheim, J. J.; Dincă, M. Humidity-Mediated Dual Ionic—Electronic Conductivity Enables High Sensitivity in MOF Chemiresistors. *J. Am. Chem. Soc.* **2024**, 146 (29), 20213—20220.
- (15) Rambabu, D.; Goossens, T.; Bakuru, V. R.; Apostol, P.; Mairesse, F.; Steenhaut, T.; Beaujean, P.; Mondal, S. K.; Guo, X.; Zhang, Y.; Pal, S.; Markowski, R.; Lin, X.; Xu, P.; Chanteux, G.; Kachmar, A.; Tie, D.; Ramackers, A.; Frano, V.; Robeyns, K.; Maji, T. K.; Filinchuk, Y.; Champagne, B.; Vlad, A. Mixed Proton-Electron Conductivity in a Dynamic 3D Metal-Organic Framework. *Chem* 2025, No. 102590.
- (16) Su, A. Y.; Apostol, P.; Wang, J.; Vlad, A.; Dincă, M. Electrochemical Capacitance Traces with Interlayer Spacing in Two-Dimensional Conductive Metal—Organic Frameworks. *Angew. Chem., Int. Ed.* **2024**, 63 (18), No. e202402526.
- (17) Lu, Y.; Zhang, Y.; Yang, C.-Y.; Revuelta, S.; Qi, H.; Huang, C.; Jin, W.; Li, Z.; Vega-Mayoral, V.; Liu, Y.; Huang, X.; Pohl, D.; Položij, M.; Zhou, S.; Cánovas, E.; Heine, T.; Fabiano, S.; Feng, X.; Dong, R. Precise Tuning of Interlayer Electronic Coupling in Layered Conductive Metal-Organic Frameworks. *Nat. Commun.* 2022, 13 (1), No. 7240.
- (18) Lu, Y.; Hu, Z.; Petkov, P.; Fu, S.; Qi, H.; Huang, C.; Liu, Y.; Huang, X.; Wang, M.; Zhang, P.; Kaiser, U.; Bonn, M.; Wang, H. I.; Samori, P.; Coronado, E.; Dong, R.; Feng, X. Tunable Charge Transport and Spin Dynamics in Two-Dimensional Conjugated Metal—Organic Frameworks. *J. Am. Chem. Soc.* **2024**, *146* (4), 2574—2582
- (19) Meyer, W. H. Polymer Electrolytes for Lithium-Ion Batteries. *Adv. Mater.* **1998**, *10* (6), 439–448.
- (20) Homann, G.; Stolz, L.; Nair, J.; Laskovic, I. C.; Winter, M.; Kasnatscheew, J. Poly(Ethylene Oxide)-Based Electrolyte for Solid-State-Lithium-Batteries with High Voltage Positive Electrodes: Evaluating the Role of Electrolyte Oxidation in Rapid Cell Failure. *Sci. Rep.* **2020**, *10* (1), No. 4390.
- (21) An, H.; Li, M.; Liu, Q.; Song, Y.; Liu, J.; Yu, Z.; Liu, X.; Deng, B.; Wang, J. Strong Lewis-Acid Coordinated PEO Electrolyte Achieves 4.8 V-Class All-Solid-State Batteries over 580 Wh kg—1. *Nat. Commun.* **2024**, *15* (1), No. 9150.
- (22) Wang, X.; Zhang, C.; Sawczyk, M.; Sun, J.; Yuan, Q.; Chen, F.; Mendes, T. C.; Howlett, P. C.; Fu, C.; Wang, Y.; Tan, X.; Searles, D. J.; Král, P.; Hawker, C. J.; Whittaker, A. K.; Forsyth, M. Ultra-Stable All-Solid-State Sodium Metal Batteries Enabled by Perfluoropolyether-Based Electrolytes. *Nat. Mater.* **2022**, *21* (9), 1057–1065.
- (23) Moro, S.; Siemons, N.; Drury, O.; Warr, D. A.; Moriarty, T. A.; Perdigão, L. M. A.; Pearce, D.; Moser, M.; Hallani, R. K.; Parker, J.; McCulloch, I.; Frost, J. M.; Nelson, J.; Costantini, G. The Effect of Glycol Side Chains on the Assembly and Microstructure of Conjugated Polymers. ACS Nano 2022, 16 (12), 21303–21314.
- (24) Roh, H.; Kim, D.-H.; Cho, Y.; Jo, Y.-M.; del Alamo, J. A.; Kulik, H. J.; Dincă, M.; Gumyusenge, A. Robust Chemiresistive Behavior in Conductive Polymer/MOF Composites. *Adv. Mater.* **2024**, *36* (27), No. 2312382.
- (25) Rivas, B. L.; Maureira, A. Poly(2-Acrylamido Glycolic Acid): A Water-Soluble Polymer with Ability to Interact with Metal Ions in Homogenous Phase. *Inorg. Chem. Commun.* **2007**, *10* (2), 151–154.
- (26) Materials Studio Dassault Systèmes. https://www.3ds.com/products/biovia/materials-studio (accessed Jun 10, 2025).
- (27) Wang, J.; Chen, T.; Jeon, M.; Oppenheim, J. J.; Tan, B.; Kim, J.; Dincă, M. Superior Charge Transport in Ni-Diamine Conductive MOFs. J. Am. Chem. Soc. 2024, 146 (29), 20500–20507.
- (28) Zasada, L. B.; Le, P. H.; Hill, A. M.; Shafranek, R. T.; Xiao, D. J. Controlling the Crystal Packing and Morphology of Metal—Organic Macrocycles through Side-Chain Modification. *ACS Mater. Lett.* **2024**, *6* (7), 3043—3049.

- (29) Le, P. H.; Zasada, L. B.; Xiao, D. J. Truncating 2D Framework Materials Down to a Single Pore: Synthetic Approaches and Opportunities. *Acc. Chem. Res.* **2025**, *58*, 1776–1785.
- (30) Siemons, N.; Pearce, D.; Cendra, C.; Yu, H.; Tuladhar, S. M.; Hallani, R. K.; Sheelamanthula, R.; LeCroy, G. S.; Siemons, L.; White, A. J. P.; McCulloch, I.; Salleo, A.; Frost, J. M.; Giovannitti, A.; Nelson, J. Impact of Side-Chain Hydrophilicity on Packing, Swelling, and Ion Interactions in Oxy-Bithiophene Semiconductors. *Adv. Mater.* **2022**, 34 (39), No. 2204258.
- (31) Moser, M.; Hidalgo, T. C.; Surgailis, J.; Gladisch, J.; Ghosh, S.; Sheelamanthula, R.; Thiburce, Q.; Giovannitti, A.; Salleo, A.; Gasparini, N.; Wadsworth, A.; Zozoulenko, I.; Berggren, M.; Stavrinidou, E.; Inal, S.; McCulloch, I. Side Chain Redistribution as a Strategy to Boost Organic Electrochemical Transistor Performance and Stability. *Adv. Mater.* **2020**, 32 (37), No. 2002748.
- (32) Meacham, R. F.; Roh, H.; Cunin, C. E.; Lee, E. R.; Li, W.; Zhao, Y.; Samal, S.; Gumyusenge, A. Contrasting Interchain Order and Mixed Ionic—Electronic Conduction in Conjugated Polymers: An Isoindigo Case Study. *RSC Appl. Polym.* **2024**, *2* (6), 1193–1201.
- (33) Kukhta, N. A.; Marks, A.; Luscombe, C. K. Molecular Design Strategies toward Improvement of Charge Injection and Ionic Conduction in Organic Mixed Ionic–Electronic Conductors for Organic Electrochemical Transistors. *Chem. Rev.* **2022**, *122* (4), 4325–4355.
- (34) Gumyusenge, A. Organic Iono-Electronics, a New Front for Semiconducting Polymers to Shine. *Acc. Mater. Res.* **2022**, 3 (7), 669–671.
- (35) Healy, C.; Patil, K. M.; Wilson, B. H.; Hermanspahn, L.; Harvey-Reid, N. C.; Howard, B. I.; Kleinjan, C.; Kolien, J.; Payet, F.; Telfer, S. G.; Kruger, P. E.; Bennett, T. D. The Thermal Stability of Metal-Organic Frameworks. *Coord. Chem. Rev.* **2020**, 419, No. 213388.
- (36) Yang, H.; Wu, N. Ionic Conductivity and Ion Transport Mechanisms of Solid-State Lithium-Ion Battery Electrolytes: A Review. *Energy Sci. Eng.* **2022**, *10* (5), 1643–1671.
- (37) Lin, D.; Liu, Y.; Cui, Y. Reviving the Lithium Metal Anode for High-Energy Batteries. *Nat. Nanotechnol.* **2017**, *12* (3), 194–206.
- (38) Bayer, T.; Bishop, S. R.; Perry, N. H.; Sasaki, K.; Lyth, S. M. Tunable Mixed Ionic/Electronic Conductivity and Permittivity of Graphene Oxide Paper for Electrochemical Energy Conversion. *ACS Appl. Mater. Interfaces* **2016**, 8 (18), 11466–11475.
- (39) Riess, I. Measurement of Ionic Conductivity in Semiconductors and Metals. *Solid State Ionics* **1991**, 44 (3), 199–205.
- (40) Wu, M.; Huang, H.; Xu, B.; Zhang, G. Poly(Ethylene Glycol)-Functionalized 3D Covalent Organic Frameworks as Solid-State Polyelectrolytes. *RSC Adv.* **2022**, *12* (26), 16354–16357.
- (41) Deslouis, C.; El Moustafid, T.; Musiani, M. M.; Tribollet, B. Mixed Ionic-Electronic Conduction of a Conducting Polymer Film. *Ac* Impedance Study of Polypyrrole. *Electrochim. Acta* **1996**, *41* (7), 1343–1349.
- (42) Riess, I. Review of the Limitation of the Hebb-Wagner Polarization Method for Measuring Partial Conductivities in Mixed Ionic Electronic Conductors. *Solid State Ionics* **1996**, *91* (3), 221–232.



CAS BIOFINDER DISCOVERY PLATFORM™

BRIDGE BIOLOGY AND CHEMISTRY FOR FASTER ANSWERS

Analyze target relationships, compound effects, and disease pathways

Explore the platform

